

Supporting Information

Gradient Defects-mediated Negative-thermal-quenching in Phosphors

Mingxue Deng,^{1,2,10} Xingzhong Cao,^{3,10} Yangmin Tang,^{1,2} Zhenzhen Zhou,^{1*} Lijia Liu,⁴ Xiaofeng Liu,⁵ Peng Zhang,³ Lo-Yueh Chang,⁶ Hao Ruan,⁷ Xinjun Guo,⁷ Jiacheng Wang,^{1,2,8,9*} Qian Liu^{1,2*}

1. State Key Laboratory of High Performance Ceramics and Superfine Microstructure, Shanghai Institute of Ceramics, Chinese Academy of Sciences, Shanghai 200050, China, E-mail: zhouzhenzhen@mail.sic.ac.cn (Z. Z); jiacheng.wang@mail.sic.ac.cn (J. W.); qianliu@mail.sic.ac.cn (Q. L.)

2. Center of Materials Science and Optoelectronics Engineering, University of Chinese Academy of Sciences, Beijing 100049, China

3. Institute of High Energy Physics, Chinese Academy of Sciences, Beijing 100049, China

4. Department of Chemistry, Western University, London, ON N6A5B7, Canada

5. School of Materials Science and Engineering, Zhejiang University, Hangzhou 310027, China

6. National Synchrotron Radiation Centre, Hsinchu, 30076, Taiwan.

7. Laboratory of Micro-Nano Optoelectronic Materials and Devices, Shanghai Institute of Optics and Fine Mechanics, Chinese Academy of Sciences, Shanghai, 201800, China

8. Hebei Provincial Key Laboratory of Inorganic Nonmetallic Materials, College of Materials Science and Engineering, North China University of Science and Technology, Tangshan 063210, China

9. School of Materials Science and Engineering, Taizhou University, Taizhou, Zhejiang, China.

10. These authors contributed equally.

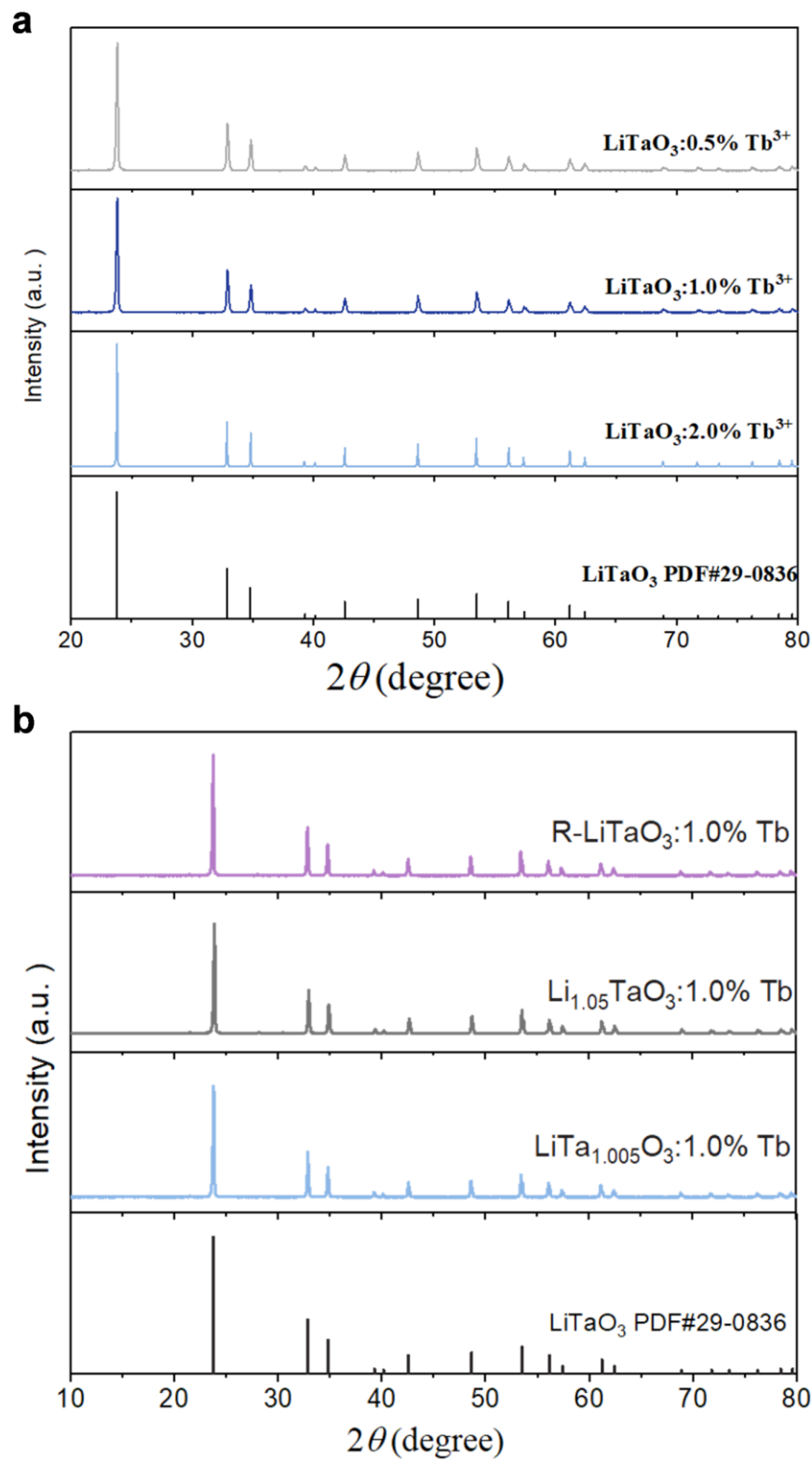


Fig. S1 XRD patterns of **a**, LiTaO_3 : $x\text{Tb}^{3+}$ ($x=0.5\%$, 1.0% and 2.0%) phosphors. **b**, LiTaO_3 : $1.0\%\text{Tb}^{3+}$ with reducing atmosphere treatment, or addition of Li or Ta alone.

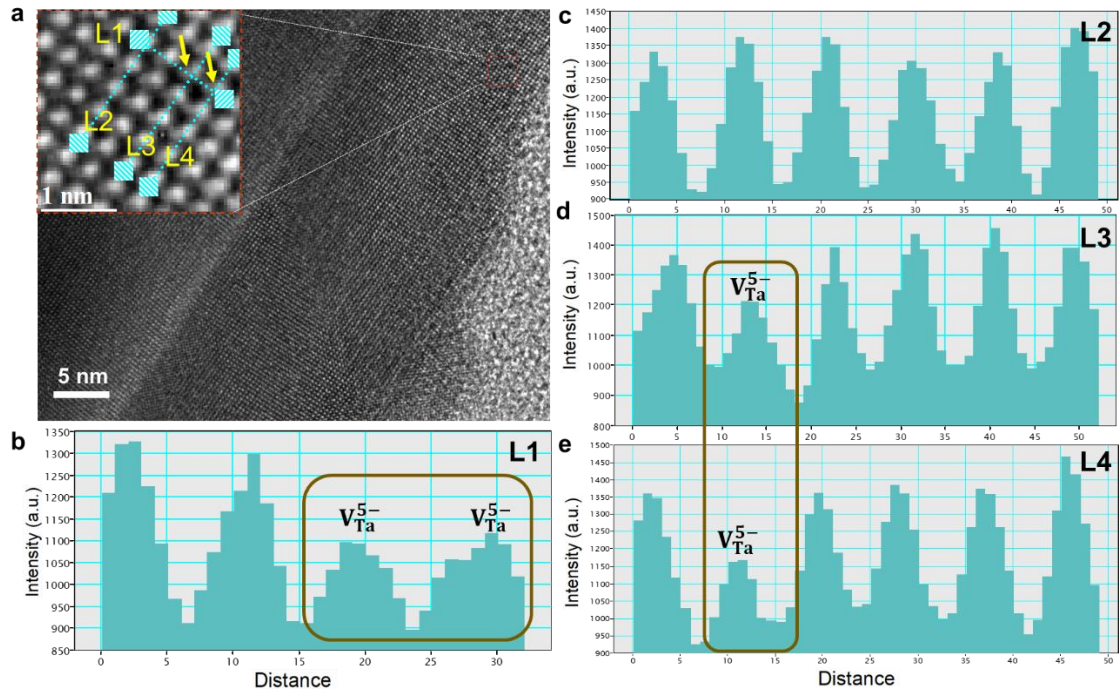


Fig. S2 a, HRTEM image of $\text{LiTaO}_3:1.0\%\text{Tb}^{3+}$ with Ta vacancy (V_{Ta}^{5-}). The inset shows a magnified Fourier-transform image of the red box region. **b-e**, Intensity profiles along the L1-L4 lines recorded from **a**. The intensity profile shows the presence of a V_{Ta}^{5-} as pointed by the yellow arrows.

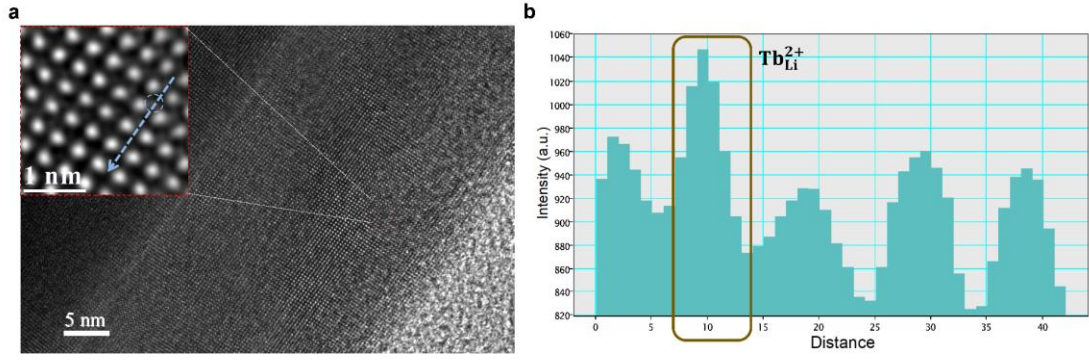


Fig. S3 a, HRTEM image of $\text{LiTaO}_3:1.0\%\text{Tb}^{3+}$ with $\text{Tb}_{\text{Li}}^{2+}$ defect. The inset shows a magnified Fourier-transform image of the red box region. **b**, Intensity profile along the blue arrow recorded from **a**, showing the existence of a $\text{Tb}_{\text{Li}}^{2+}$ defect as illustrated in brown box.

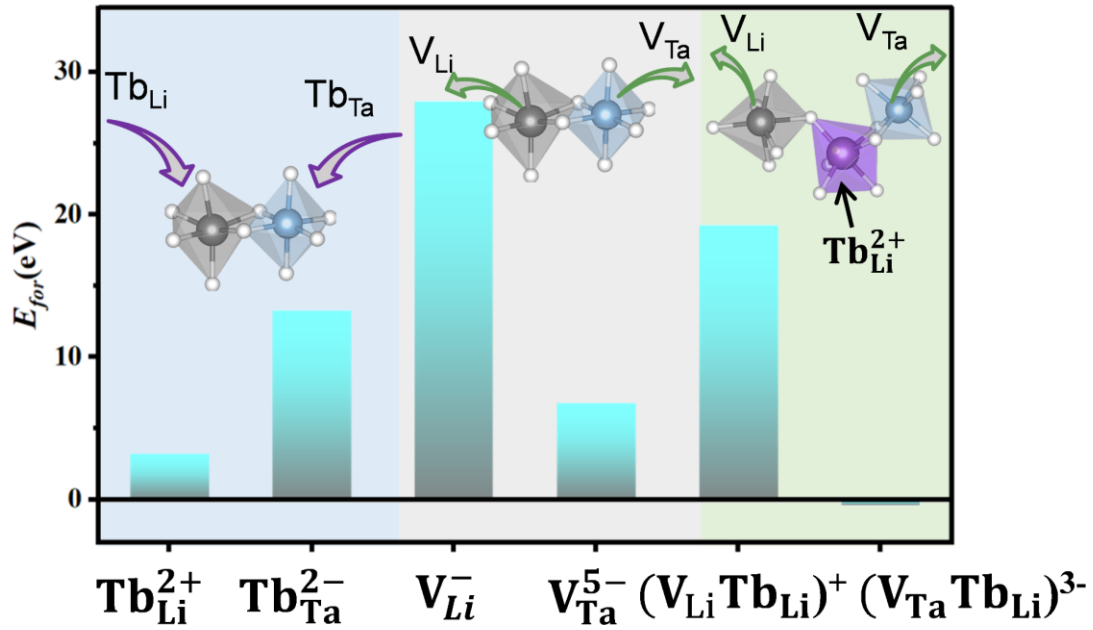


Fig. S4 The formation energies (E_{for}) of LiTaO₃ with different defects determined by DFT calculation. The inset shows the corresponding structural models, where white, grey and light blue spheres represent elements Li, Ta, O, and Tb, respectively. The results depict that Tb atom occupies Li site preferentially. Moreover, $r(Li^+, CN6)$ is 0.76 Å, $r(Ta^{5+}, CN6)$ is 0.64 Å, and $r(Tb^{3+}, CN6)$ is 0.92 Å. From the perspective of ion radius, the dopants Tb^{3+} ions with a large radius are easier to enter the Li^+ lattice sites. Both V_{Ta}^{5-} and complex-defect $(V_{Ta} Tb_{Li})^{3-}$ have lower formation energies than V_{Li}^- and $(V_{Li} Tb_{Li})^+$. Thus, DFT calculation explains the tendency of the formation of triple defects, including Tb_{Li}^{2+} , V_{Ta}^{5-} and complex-defect $(V_{Ta} Tb_{Li})^{3-}$, from the thermodynamic point of view.

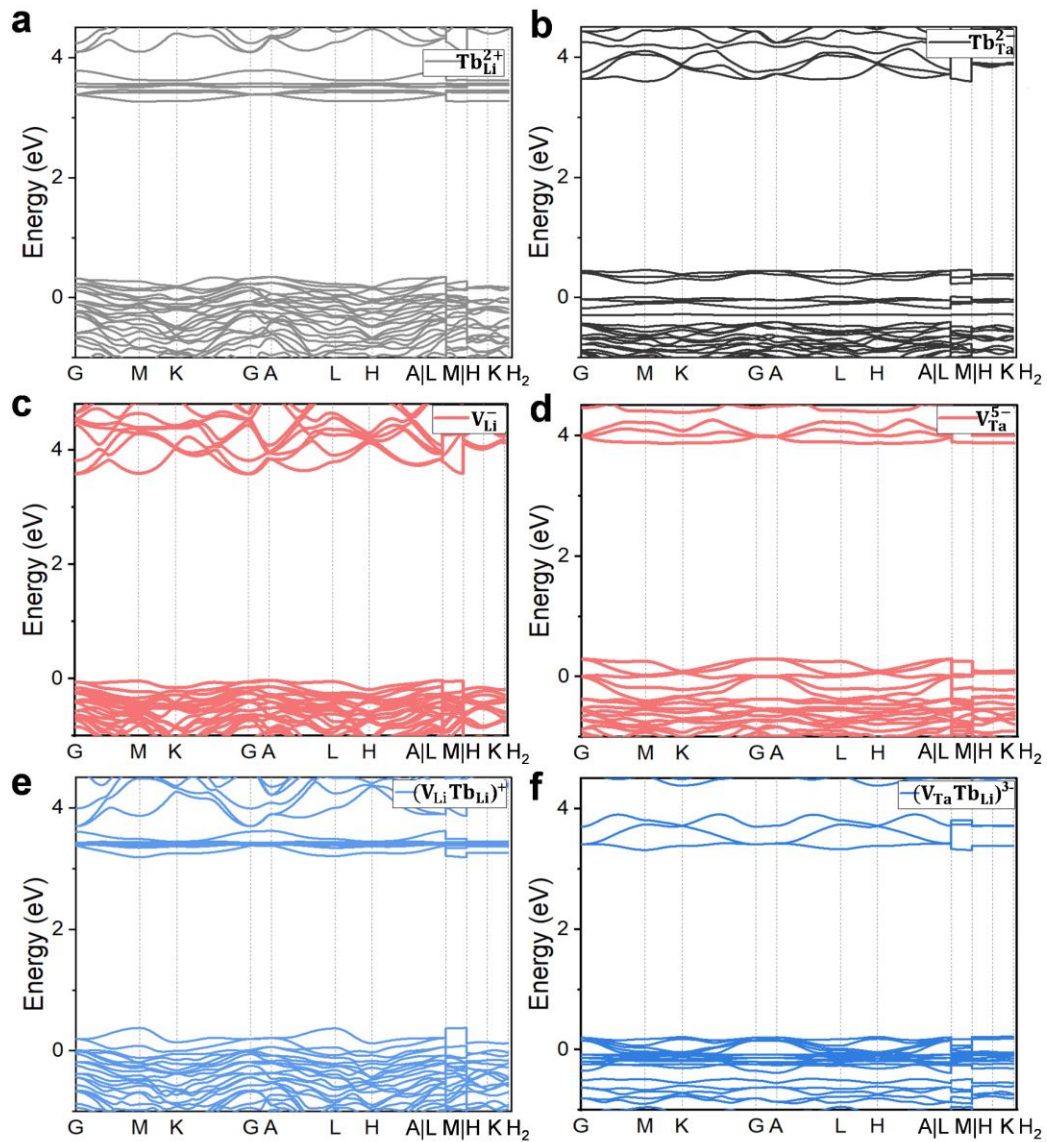


Fig. S5 Electronic band structures of LiTaO_3 with different defects calculated by density functional theory (DFT) calculations.

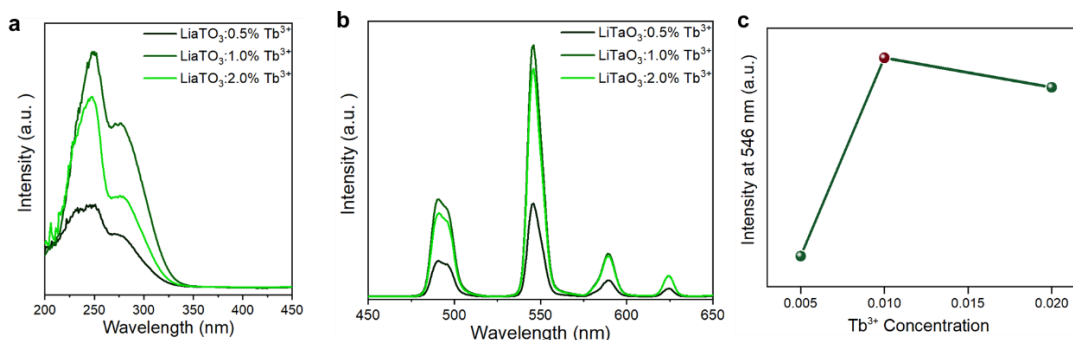


Fig. S6 a, PLE and **b**, PL spectra of $\text{LiTaO}_3:x\text{Tb}^{3+}$ ($x=0.5\%$, 1.0% , and 2.0%) phosphors. **c**, PL intensity at 546 nm as a function of Tb^{3+} concentration.

Fig. S6 shows the excitation and emission spectra of the $\text{LiTaO}_3:x\text{Tb}^{3+}$ ($x=0.5\%$, 1.0% , and 2.0%) phosphors. PLE spectra monitored at 546 nm exhibit a slightly wider band with two peaks at 250 and 290 nm, respectively, which are derived from host absorbance and spin-allowed $4f \rightarrow 5d$ transition of Tb^{3+} . Upon 250 nm excitation, $\text{LiTaO}_3:x\text{Tb}^{3+}$ ($x=0.5\%$, 1.0% and 2.0%) phosphors exhibit a series of sharp emission peaks, due to transitions from 5D_4 level to the 7F_j ($j=6, 5, 4, 3$) ground state. With the increase of Tb concentration, the intensity of PL increases first and then decreases slightly, and reaches the maximum at 1% doping concentration. It can be explained by concentration quenching.

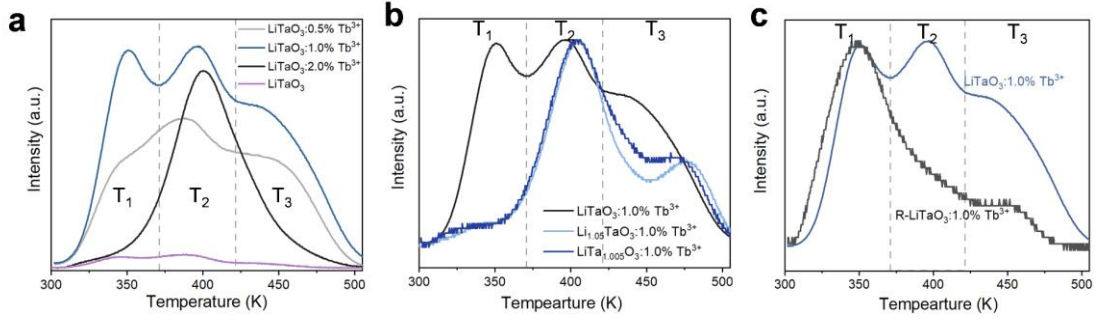


Fig. S7 a, TL spectra of $\text{LiTaO}_3:x\text{Tb}^{3+}$ ($x=0, 0.5\%, 1.0\%$ and 2.0%) phosphors. **b**, TL spectra of $\text{LiTaO}_3:1.0\%\text{Tb}^{3+}$ phosphors with excessive of Li or Ta. **c**, TL spectra of $\text{LiTaO}_3:1.0\%\text{Tb}^{3+}$ phosphors with and without reducing atmosphere treatment.

As the concentration of Tb^{3+} increases, growing amount of Tb^{3+} ions occupies Li^+ sites to form more $\text{Tb}_{\text{Li}}^{2+}$ defects. In order to balance the charge, the concentration of $\text{V}_{\text{Ta}}^{5-}$ and complex-defect $(\text{V}_{\text{Ta}}\text{Tb}_{\text{Li}})^{3-}$ increases correspondingly, reaching the maximum for the $\text{LiTaO}_3:1.0\%\text{Tb}^{3+}$ phosphor (Fig. S7a). High-concentration doping may cause Tb^{3+} to occupy other positions, thus resulting in the decrease of $\text{V}_{\text{Ta}}^{5-}$. The supplementation of Li or Ta could make Li or Ta occupy the Ta position. Thus, it leads to the significant decrease of the defect $\text{V}_{\text{Ta}}^{5-}$ and has little effect on the defect $\text{Tb}_{\text{Li}}^{2+}$ (Fig. S7b). Therefore, it is reliable to speculate that T_2 is ascribed to $\text{Tb}_{\text{Li}}^{2+}$. The reduction atmosphere treatment was also used to create more positively charged oxygen vacancies, leading to the decrease of the corresponding positively charged defect $\text{Tb}_{\text{Li}}^{2+}$ as well as complex-defect $(\text{V}_{\text{Ta}}\text{Tb}_{\text{Li}})^{3-}$. However, the negative charge $\text{V}_{\text{Ta}}^{5-}$ increases slightly or remains unchanged (Fig. S7c). From this, we can infer that T_1 is ascribed to the defect $\text{V}_{\text{Ta}}^{5-}$ and T_3 is due to complex-defect $(\text{V}_{\text{Ta}}\text{Tb}_{\text{Li}})^{3-}$. Combined with XPS of Ta 4f, the negative offset of Ta 4f increases first and then decreases with the concentration, which means the Ta vacancy increases first and then decreases. Moreover, after 5%Li supplementation, the negative offset decreases compared with that $\text{LiTaO}_3:1.0\%\text{Tb}^{3+}$, which means the decrease of $\text{V}_{\text{Ta}}^{5-}$. It is further confirmed that T_1 is related to $\text{V}_{\text{Ta}}^{5-}$.

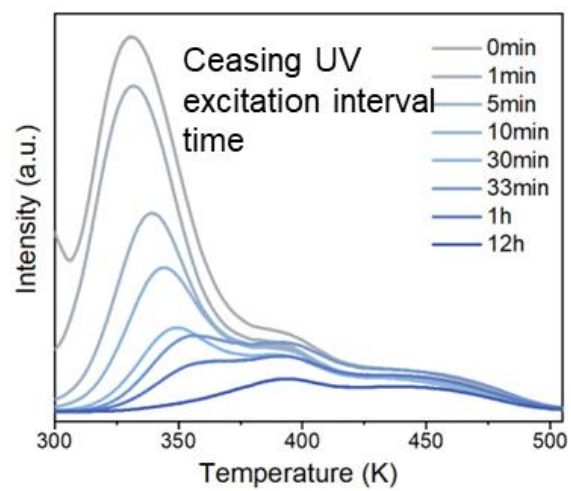


Fig. S8 TL spectra of LiTaO₃:1.0% Tb³⁺ recorded at different intervals after ceasing UV excitation.

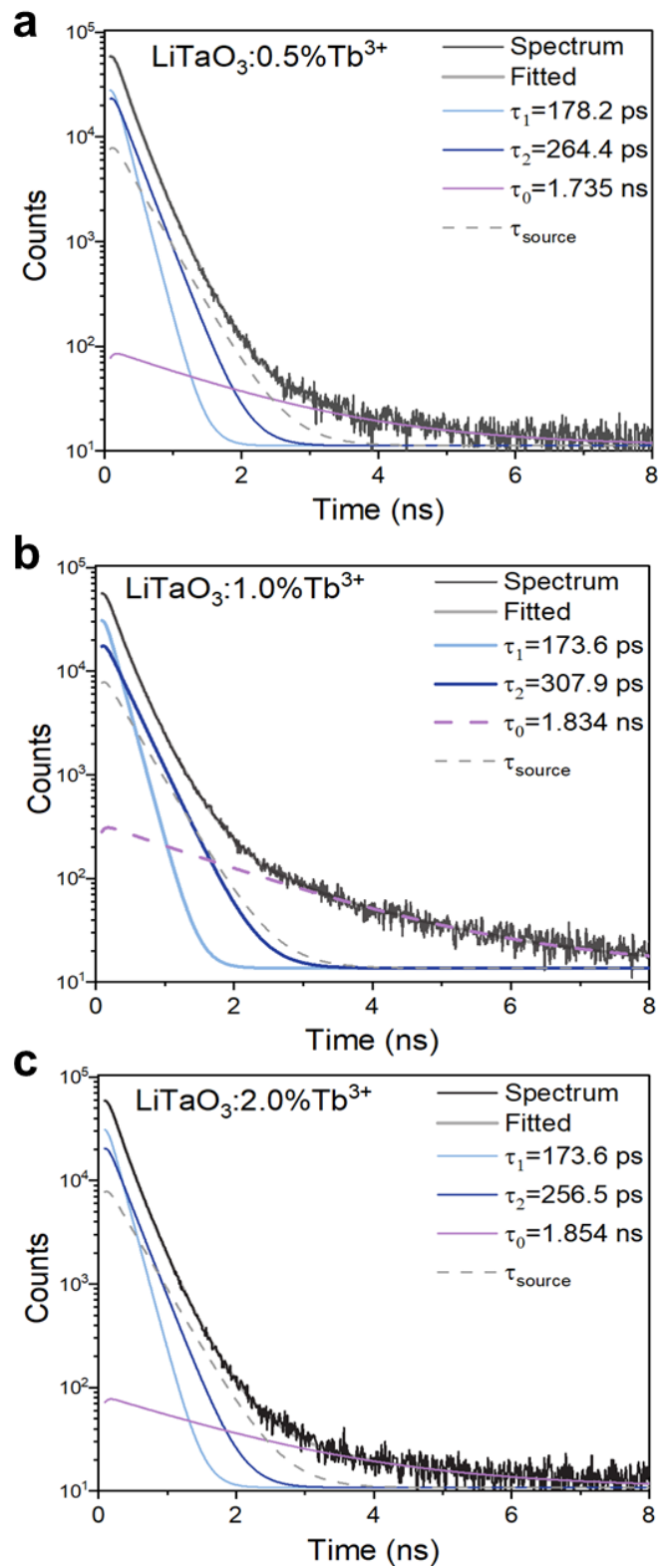


Fig. S9 Experimental positron annihilation lifetime spectra with deconvoluting components of **a**, $\text{LiTaO}_3:0.5\%\text{Tb}^{3+}$, **b**, $\text{LiTaO}_3:1.0\%\text{Tb}^{3+}$, and **c**, $\text{LiTaO}_3:2.0\%\text{Tb}^{3+}$.

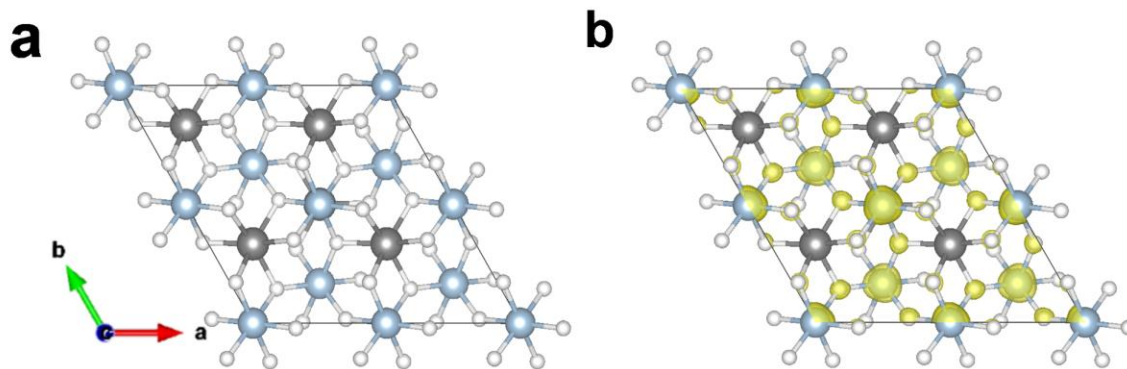


Fig. S10 a, Schematic diagram of the crystal structure, and **b**, defect trapping positron in perfect LiTaO₃ lattice. Yellow represents the positron accumulation. Isosurface level is 0.000005, far less than the positron density in the structure with defects.

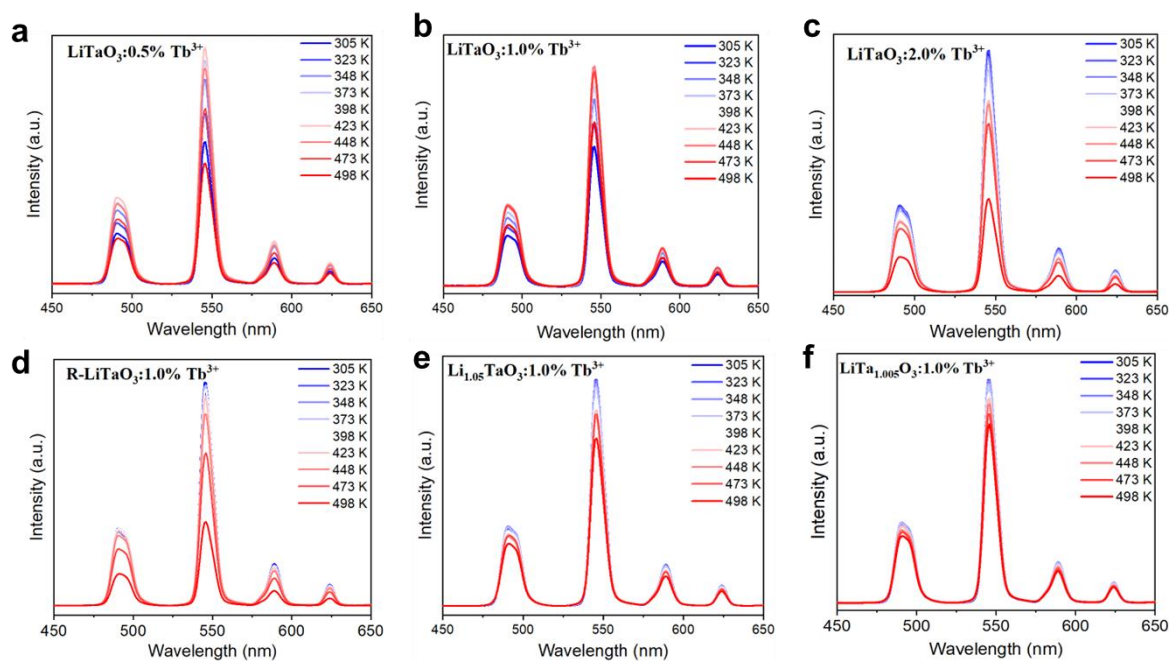


Fig. S11 Temperature-dependent emission spectra of **a**, LiTaO₃:0.5%Tb³⁺, **b**, LiTaO₃:1.0%Tb³⁺, **c**, LiTaO₃:2.0%Tb³⁺, **d**, R-LiTaO₃:1.0%Tb³⁺, **e**, Li_{1.05}TaO₃:1.0%Tb³⁺, and **f**, LiTa_{1.005}O₃:1.0%Tb³⁺.

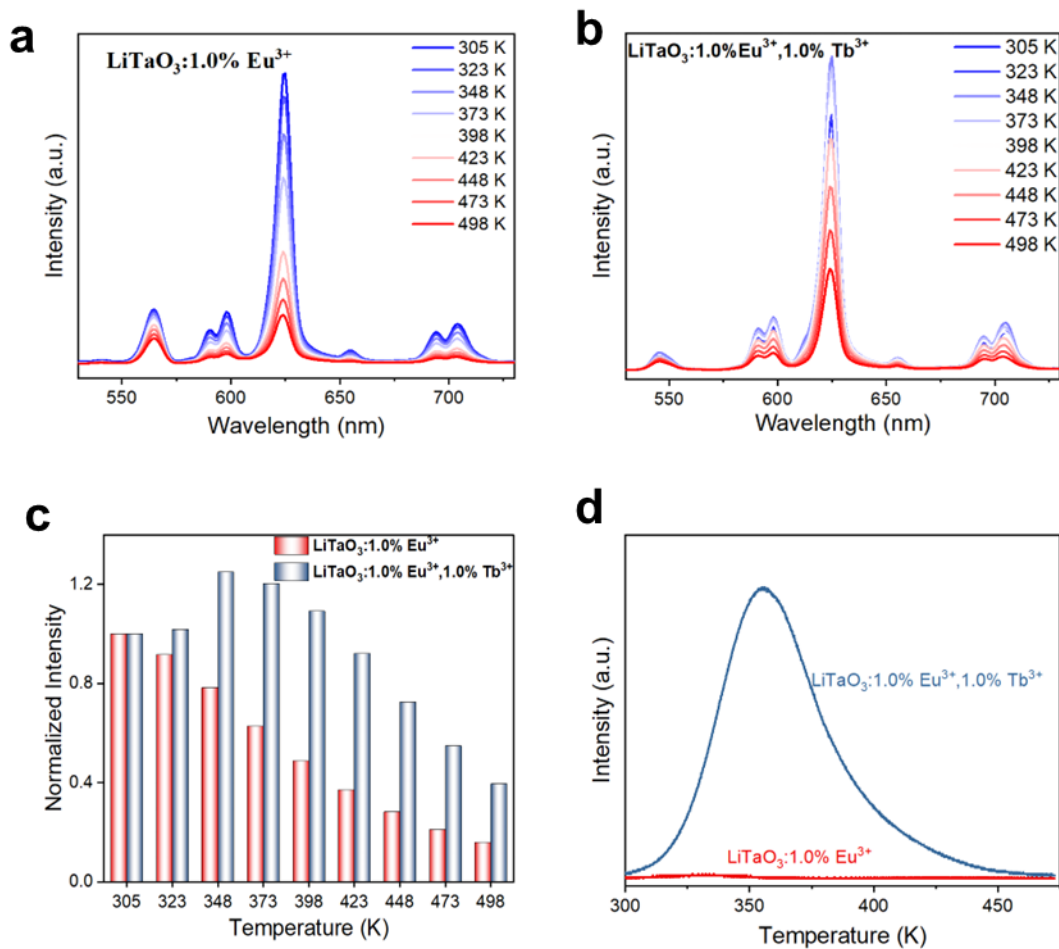


Fig. S12. **a, b,** Temperature-dependent emission spectra of single-doped $\text{LiTaO}_3:1.0\% \text{Eu}^{3+}$ and co-doped $\text{LiTaO}_3:1.0\% \text{Eu}^{3+}, 1.0\% \text{Tb}^{3+}$ recorded at temperatures from 305 to 498 K. **c,** Normalized temperature-dependent intensity of emission at 500 nm. **d,** TL spectra of $\text{LiTaO}_3:1.0\% \text{Eu}^{3+}$ and $\text{LiTaO}_3:1.0\% \text{Eu}^{3+}, 1.0\% \text{Tb}^{3+}$ phosphors.

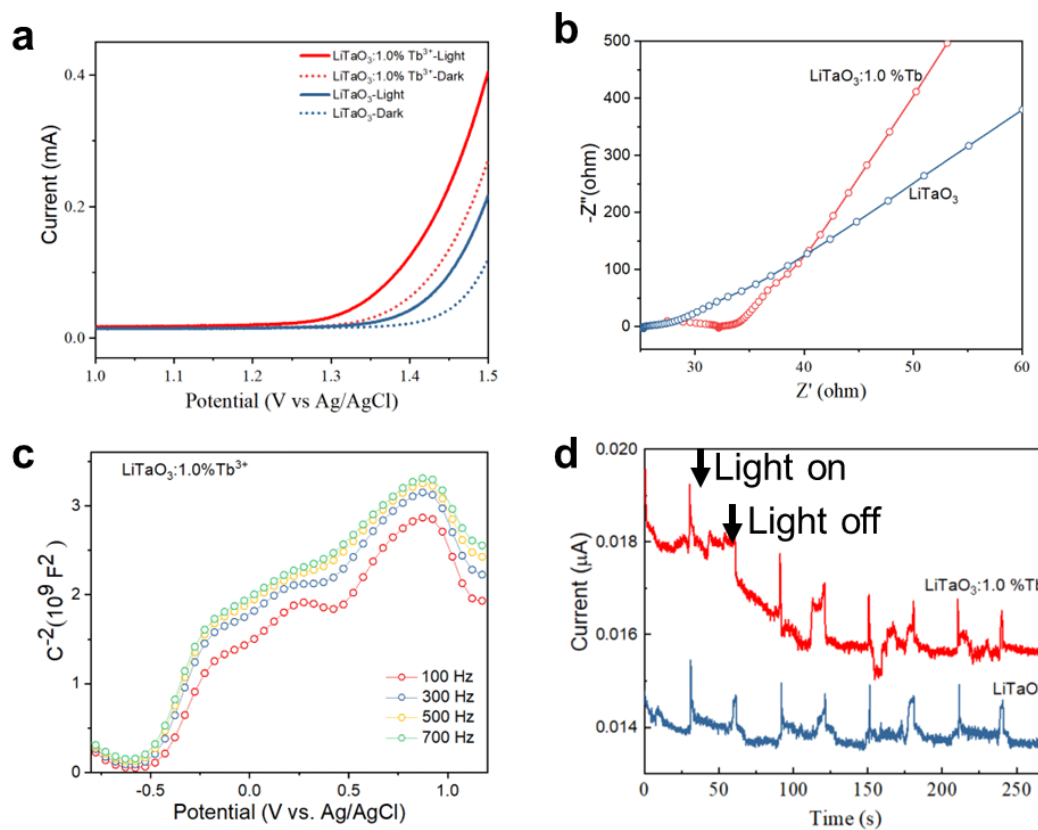


Fig. S13 a, LSV curves (in 0.2 M Na₂SO₄) of LiTaO₃:1.0%Tb³⁺ and LiTaO₃ in the dark and with light. **b**, Electrochemical impedance spectroscopy (EIS). **c**, Nyquist plots of LiTaO₃:1.0%Tb³⁺. **d**, Photocurrent responses recorded under light on and off conditions.

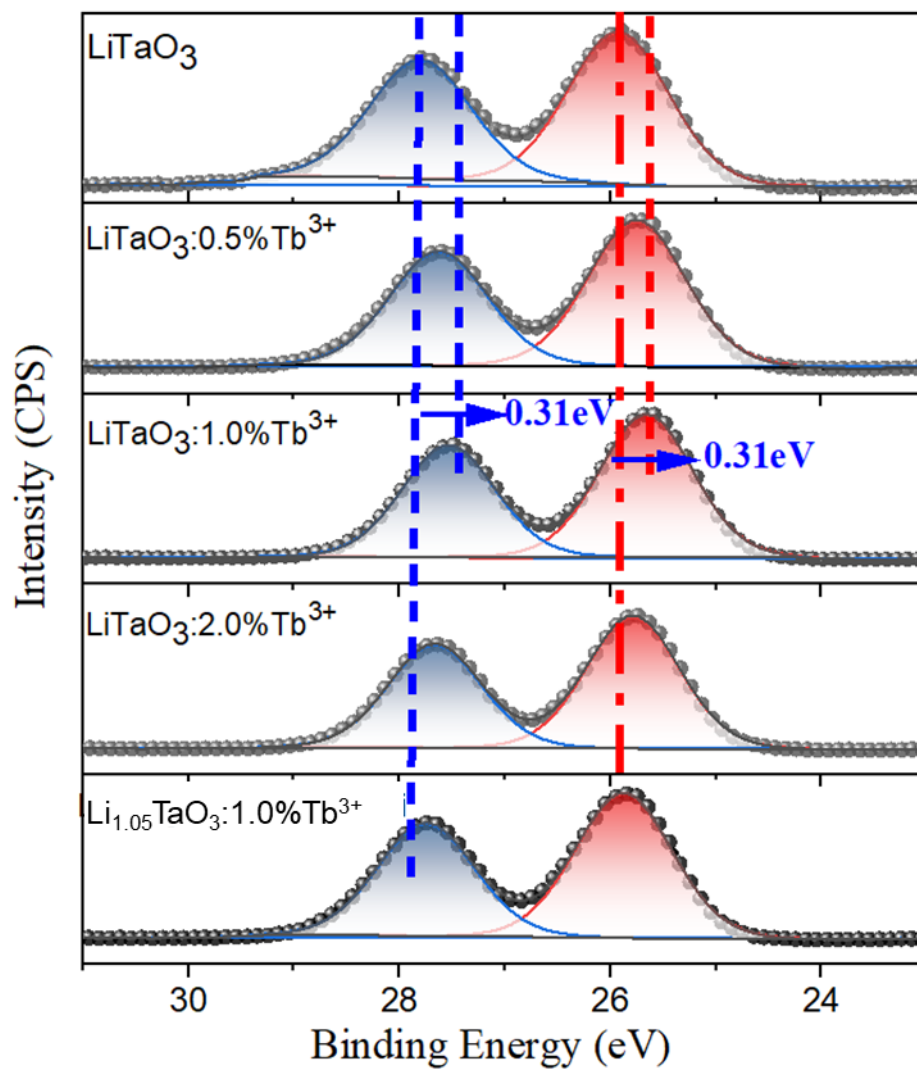


Fig. S14 High-resolution Ta 4f XPS spectra of LiTaO₃:xTb³⁺ ($x=0, 0.5\%, 1.0\%$, and 2.0%) and Li_{1.05}TaO₃:xTb³⁺.

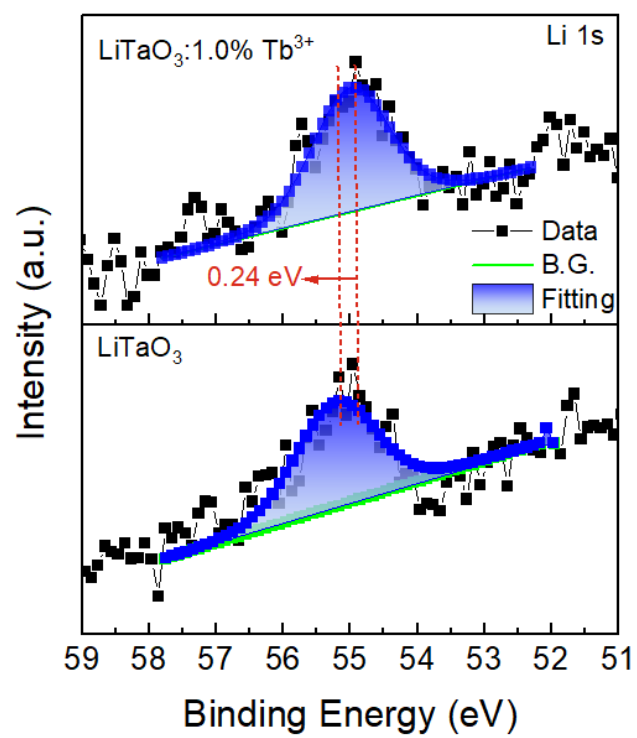


Fig. S15 High-resolution Li 1s XPS spectra of $\text{LiTaO}_3:1.0\% \text{Tb}^{3+}$ and LiTaO_3 .

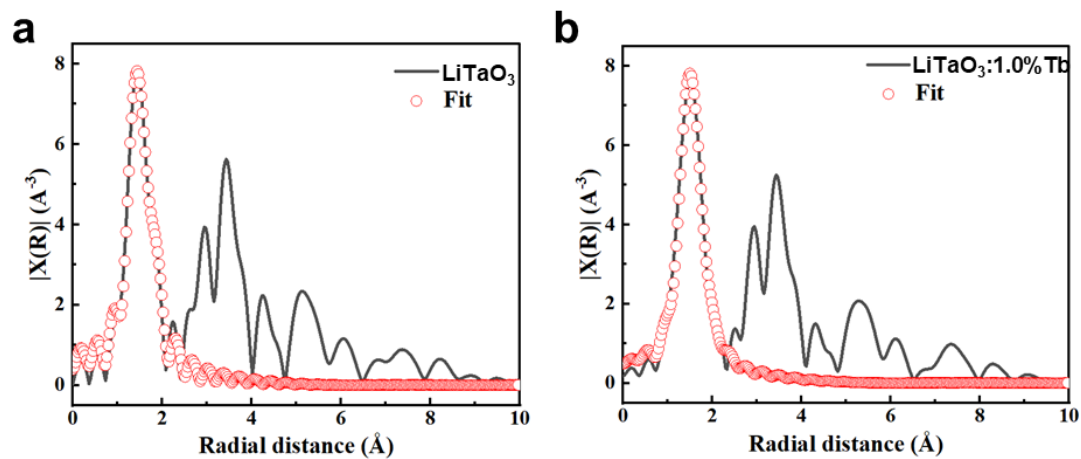


Figure S16. a, b, Ta L_{III} -edge EXAFS and fitting curves of LiTaO_3 and $\text{LiTaO}_3:1.0\% \text{Tb}^{3+}$.

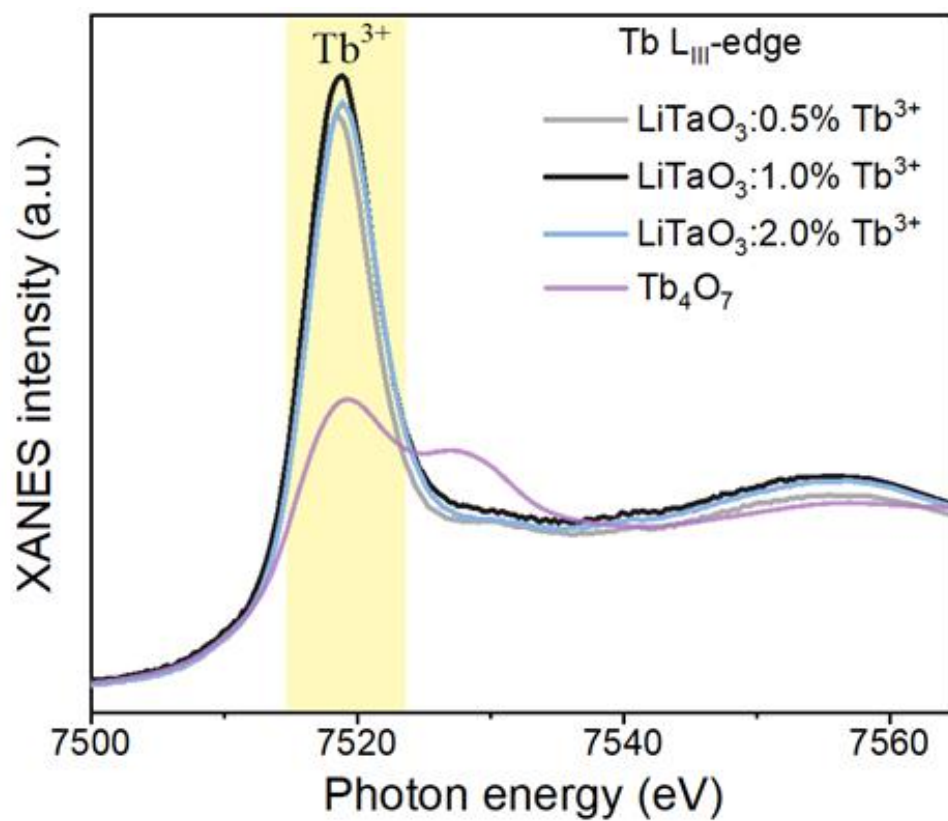


Fig. S17 XANES spectra of the Tb L_{III}-edge, recorded for LiTaO₃:xTb³⁺ ($x=0.5\%$, 1.0% and 2.0%) phosphors and Tb₄O₇ reference samples.

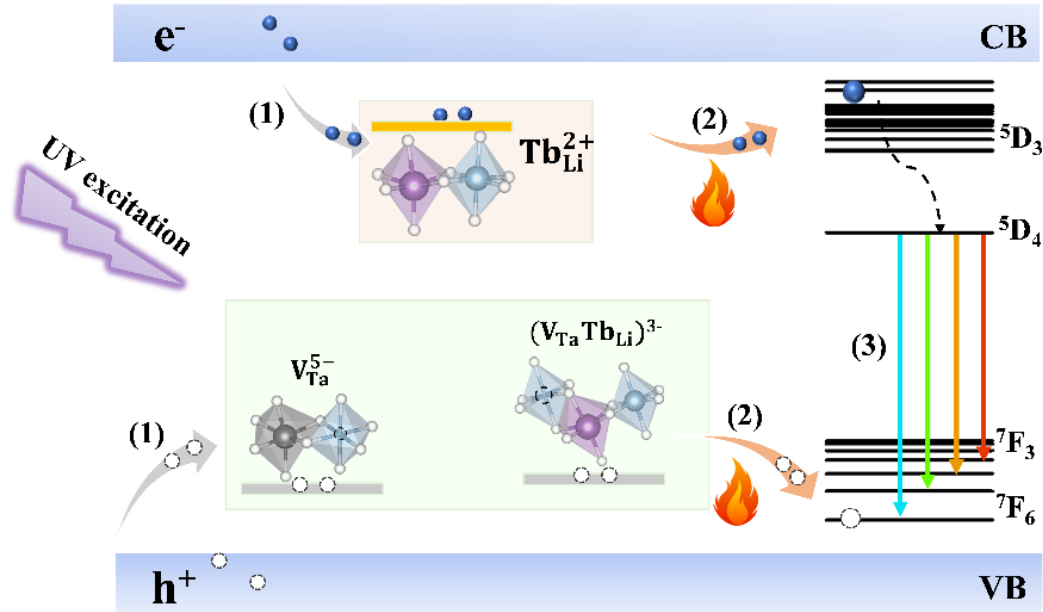


Fig. S18 Proposed mechanism of negative thermal quenching of Tb³⁺-doped LiTaO₃ with triple defects. Based on the experimental and computational results, we propose the following mechanism to explain the wide range of negative thermal quenching in Tb³⁺-doped phosphors. In LiTaO₃:1.0%Tb³⁺ phosphors, there are three types of defects that can capture carriers (electrons and holes) activated by UV light. The carriers in the defect is de-captured to compensate the heat loss upon thermal stimulation, thus achieving negative thermal quenching at high temperatures. Specifically, V_{Ta}⁵⁻ and (V_{Ta}Tb_{Li})³⁻ act as hole traps (h-traps), while Tb_{Li}²⁺ as electron traps. Under UV excitation, electrons and holes in the material could be separated, and holes in the valence band (VB) are captured by the hole trap-V_{Ta}⁵⁻ and (V_{Ta}Tb_{Li})³⁻, and electrons in the conduction band (CB) are captured by the electron trap-Tb_{Li}²⁺, as shown in process (1). In the low-temperature region (300-373 K), holes in the shallowest trap V_{Ta}⁵⁻ are firstly de-captured to the luminescence centers (Tb³⁺) (process (2)), and then holes and electrons recombine to generate luminescence (process (3)). In the mid-temperature region (373-425 K), the electrons stored in the trap of Tb_{Li}²⁺ escape to the excited state level of Tb³⁺ and release energy in the form of luminescence. In the high temperature region (425-475 K), the holes stored in the composite defect (V_{Ta}Tb_{Li})³⁻ are released to compensate the heat loss and thus leads to the negative thermal quenching behavior.

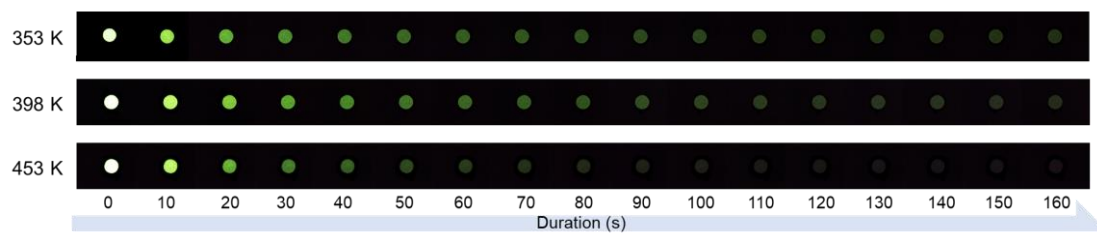


Fig. S19 Decrypting information photos with the change of heating time and heating temperature. After five minutes of UV charging, the heating time from 0-160s is controlled to realize the complete decryption of information.

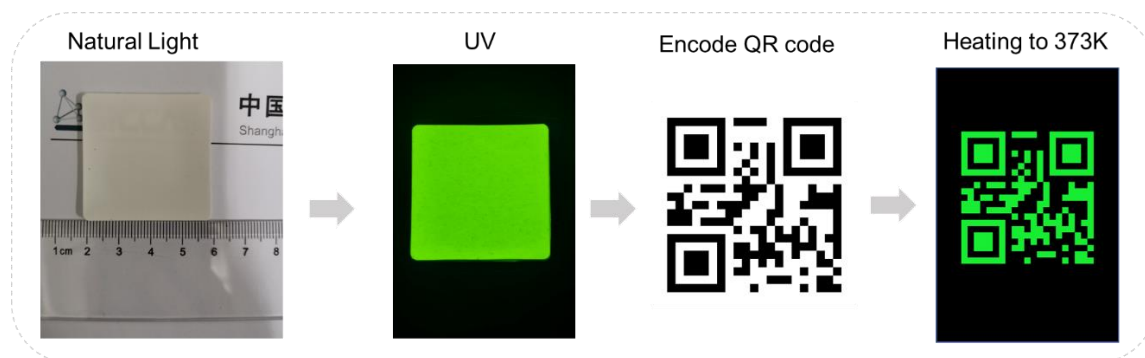


Fig. S20 A phosphor film with $\text{LiTaO}_3:1.0\%\text{Tb}^{3+}$ for encryption process and photos of two-dimensional code pattern information.

Fig. S20 demonstrates the process of using a thin phosphor film for QR code encryption. The QR code encrypted by ultraviolet light is invisible at room temperature. Increasing the temperature results in the releasing of the carriers out of the defects to generate light emission, thus the two-dimensional code becomes visible.



Fig. S21 The process and photos of encrypting and decrypting letters, numbers, and patterns using the $\text{LiTaO}_3:1.0\%\text{Tb}^{3+}$ phosphor.

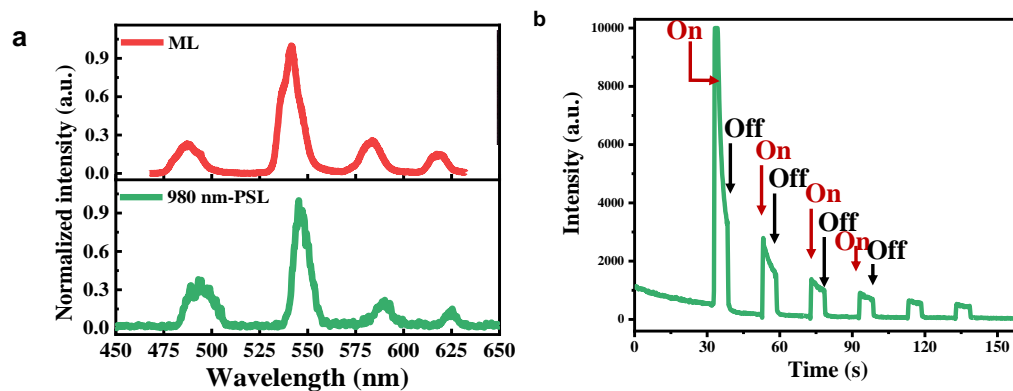


Fig. S22 a, Mechanoluminescence (ML) and photo-stimulated luminescence (PSL) spectra. **b**, The luminous intensity versus time curve when the 980 nm laser as the excitation source was repeatedly switched on and off. Before testing, the sample was charged by UV radiation.

Table S1. Refinement parameters and crystallographic data of LiTaO₃:1.0% Tb³⁺.

| Atoms | x | y | z | Occ. | U | Site | Sym. |
|-------|---------|---------|---------|-------|-------|------|------|
| Li | 0.00000 | 0.00000 | 0.29100 | 1.000 | 0.000 | 6a | 3 |
| Ta | 0.00000 | 0.00000 | 0.00000 | 1.005 | 0.005 | 6a | 3 |
| O | 0.04800 | 0.34400 | 0.06860 | 1.005 | 0.005 | 18b | 1 |
| Tb | 0.00000 | 0.00000 | 0.29100 | 0.000 | 0.000 | 6a | 3 |

Symmetry: hexagonal, space group: $R3c$, $a = b = 5.1527 \text{ \AA}$, $c = 13.7466 \text{ \AA}$,
 $V = 316.078997 \text{ \AA}^3$, $\alpha = \beta = 90^\circ$, $\gamma = 120^\circ$

Table S2. Experimental positron lifetime component results for $\text{LiTaO}_3:x\text{Tb}^{3+}$ ($x=0, 0.5\%, 1.0\%$ and 2.0%) phosphors.

| Samples | τ_1 (ps) | I_1 (%) | τ_2 (ps) | I_2 (%) | τ_0 (ns) | I_0 (%) | Error factor | τ_{aver} (ps) |
|--------------------------------------|---------------|-----------|---------------|-----------|---------------|-----------|--------------|---------------------------|
| $\text{LiTaO}_3:0.5\%\text{Tb}^{3+}$ | 178.2 | 57.6 | 264.4 | 41.7 | 1.7 | 0.7 | 1.0197 | 224.5 |
| $\text{LiTaO}_3:1.0\%\text{Tb}^{3+}$ | 173.6 | 54.7 | 307.9 | 42.4 | 1.8 | 1.8 | 1.0942 | 279.0 |
| $\text{LiTaO}_3:2.0\%\text{Tb}^{3+}$ | 173.6 | 55.10 | 256.5 | 44.2 | 1.8 | 0.7 | 1.0357 | 226.0 |

Table S3. Calculated positron state lifetimes (ps) of LiTaO₃ with two kinds of negative charge defect.

| Defects | Calculated positron state lifetimes (ps) |
|-------------------------|--|
| V_{Ta}^{5-} | 173.8 |
| $(V_{Ta} Tb_{Li})^{3-}$ | 299.0 |

Table S4. The fitting parameters of the Ta L_{III}-edge EXAFS curves

| Sample | Path | CN | R (Å) | σ^2 (Å²) | E₀ (eV) | R-factor |
|--|-------------|-----------|--------------|--|---------------------------|-----------------|
| LiTaO ₃ | Ta-O(1) | 2.9 | 1.888 | 0.0015 | 5.95 | 0.007 |
| | Ta-O(2) | 2.6 | 2.047 | 0.0015 | | |
| LiTaO ₃ :1.0%Tb ³⁺ | Ta-O(1) | 3.2 | 1.899 | 0.0035 | 7.67 | 0.005 |
| | Ta-O(2) | 2.6 | 2.046 | 0.0035 | | |

CN is coordination number, E₀ is edge-energy shift, σ^2 is Debye-Waller factor.